



Cite this: *RSC Adv.*, 2022, **12**, 20583

## Feasibility study of Mg storage in a bilayer silicene anode *via* application of an external electric field<sup>†</sup>

Sumaiyatul Ahsan,<sup>‡,a</sup> Abrar Rauf,<sup>‡,a</sup> M. F. N. Taufique,<sup>‡,b</sup> Hasan Al Jame,<sup>a</sup> Saugata Sarker,<sup>a</sup> Sadiq Shahriyar Nishat,<sup>c</sup> Md Tohidul Islam,<sup>d</sup> Azmain Faek Islam,<sup>e</sup> Md Rafsun Jani,<sup>a</sup> Md Shafiqul Islam,<sup>a</sup> Kazi Md Shorowordi<sup>a</sup> and Saquib Ahmed<sup>‡,f\*</sup>

With the goal of developing a Si-based anode for Mg-ion batteries (MIBs) that is both efficient and compatible with the current semiconductor industry, the current research utilized classical Molecular Dynamics (MD) simulation in investigating the intercalation of a  $Mg^{2+}$  ion under an external electric field (E-field) in a 2D bilayer silicene anode (BSA). First principles density functional theory calculations were used to validate the implemented EDIP potentials. Our simulation shows that there exists an optimum E-field value in the range of 0.2–0.4 V  $\text{\AA}^{-1}$  for  $Mg^{2+}$  intercalation in BSA. To study the effect of the E-field on  $Mg^{2+}$  ions, an exhaustive spread of investigations was carried out under different boundary conditions, including calculations of mean square displacement (MSD), interaction energy, radial distribution function (RDF), and trajectory of ions. Our results show that the  $Mg^{2+}$  ions form a stable bond with Si in BSA. The effects of E-field direction and operating temperature were also investigated. In the X–Y plane in the 0°–45° range, 15° from the X-direction was found to be the optimum direction for intercalation. The results of this work also suggest that BSA does not undergo drastic structural changes during the charging cycles with the highest operating temperature being  $\sim$ 300 K.

Received 17th April 2022  
 Accepted 10th July 2022

DOI: 10.1039/d2ra02475f  
[rsc.li/rsc-advances](http://rsc.li/rsc-advances)

## 1 Introduction

The 21<sup>st</sup> century marked a rapid adoption of electrochemical energy storage in all walks of life – this fact in turn calls for the immediate development of next-generation batteries. Rechargeable lithium-ion batteries (LIBs), which are undoubtedly the most popular energy storing devices, are no longer able to adequately meet the required energy or safety requirements;<sup>1–3</sup> additionally, large-scale production of LIBs is

dependent on raw materials produced in countries with geopolitical risks.<sup>4</sup> Among post-LIB alternatives,<sup>5–7</sup> rechargeable magnesium-ion batteries (MIBs) offer the best replacement technology. MIBs utilize divalent  $Mg^{2+}$  as charge carriers, which have smaller ionic radii than  $Li^+$  while offering a higher volumetric energy density due to their capability of storing two electrons per ion, and the natural advantage of utilizing earth-abundant materials.<sup>5,6,8–11</sup> Mg undergoes safer reversible dendrite-free deposition in Mg metal anodes<sup>5,6,11</sup> which is why most research on MIBs is done utilizing metallic Mg anodes, with a focus on developing the cathode materials<sup>10,12</sup> and electrolytes.<sup>10</sup>

Despite all the benefits of metallic Mg anode, it is impractical for practical usage due to its incompatibility with conventional electrolytes used in batteries. It can result in undesirable electrode–electrolyte reactions, resulting in the formation of a blocking layer<sup>12</sup> and leading to poor cycling ability and battery voltage. To solve this issue, a large focus of current MIB research has been on developing an anode material that is compatible with conventional battery materials,<sup>13–19</sup> instead of developing new electrolytes and cathode. There is no doubt that a critical requirement for the success of the MIB technology is in the development of a suitable anode material.

Due to the high natural abundance of silicon and its synergy with existing electrochemical and semiconductor industry, Si-based anode is a very attractive material for the MIB technology. Many variations of Si-based anode are currently being

<sup>a</sup>Department of Materials and Metallurgical Engineering (MME), Bangladesh University of Engineering and Technology (BUET), East Campus, Dhaka, 1000, Bangladesh

<sup>b</sup>Pacific Northwest National Laboratory, Richland, WA 99354, USA

<sup>c</sup>Department of Materials Science and Engineering (MSE), Rensselaer Polytechnic Institute, 110 8th Street, Troy, NY 12180, USA

<sup>d</sup>Department of Materials Design and Innovation, University at Buffalo, Buffalo, NY 14260, USA

<sup>e</sup>School of Mechanical and Materials Engineering, Washington State University, Pullman, Washington 99163, USA

<sup>f</sup>Department of Mechanical Engineering Technology, SUNY – Buffalo State, 1300 Elmwood Avenue, Buffalo, NY 14222, USA. E-mail: ahmedsm@buffalostate.edu; Fax: +1-716-878-3033; Tel: +1-716-878-6006

<sup>†</sup> Electronic supplementary information (ESI) available: Detailed information on thermostating, smooth and unsmoothed curves and trajectories generated by using Nose–Hoover and modified NVT thermostats and unsmoothed curves using CSV thermostats. Crystallographic information file (cif) on bilayer silicene, and all experimental data from simulation is provided. See <https://doi.org/10.1039/d2ra02475f>

<sup>‡</sup> Sumaiyatul Ahsan and Abrar Rauf equally contributed to this work.



tested such as bulk Si,<sup>13</sup> nano-Si,<sup>16</sup> Al doped Si<sup>20</sup> etc. In our current investigation, we probe 2D bilayer silicene, which is a 2D allotrope of silicon (similar to graphene being the 2D allotrope of carbon). The reasons behind our choice of material are three-fold.

Firstly, most other variations of Si-based anode for MIBs have been tested already either theoretically or experimentally and found inadequate in resolving the storage problem.<sup>13,16,20</sup> Even though bulk Si might seem very promising<sup>13</sup> due to having a very high specific capacity (3817 mA hg<sup>-1</sup>) and low average insertion voltage (close to 0.15 eV vs. Mg), for Mg storage, it shows a very significant lattice expansion (nearly 216%). Mg intercalation into nano-Si anode has been proven to be inadequate,<sup>15,21</sup> and this will be further discussed in later sections.

Secondly, there exists a strong correlation between lowering the particle size of the anode particle and enhancing the intercalation process in MIBs. Strong evidence in favour of size reduction of anode particles was highlighted through a study utilizing nano-Sn anode for MIBs, where commercial Sn nanoparticles ( $\sim$ 150 nm) were shown to take up to  $\sim$ 3 weeks to store Mg. By decreasing the particle size to sub-50 nm range, this charging process time dramatically decreased to a few hours.<sup>15,16,21</sup> This correlation between size and performance can easily be explained. Mg storage in silicon is a diffusion-controlled process and the divalent nature of Mg already results in a sluggish diffusion process compared to monovalent counterparts (Li, Na). This means that lowering the characteristic particle size for anodes is critical to decreasing lattice expansion, increasing diffusion & storage rate. A similar experimental study in search for the critical size for nano-Si anode for MIBs was done to address the drawbacks associated with bulk Si;<sup>16</sup> it was shown that for oxide-free nanostructured Si with size in the range of  $\sim$ 100 nm, roughly 91.7% of Mg was removed during deintercalation. This result demonstrated a successful electrochemical path for deintercalation of Mg from nano-Si. Unfortunately, so far, attempts to reverse the process by electrochemically storing (intercalation) Mg in nano-Si anode during charging have been unsuccessful. These failures have been attributed to the relatively larger nano Si particle sizes ( $\sim$ 100 nm) compared to nano-Sn ( $\sim$ 30–50 nm) that does show successful Mg storage.<sup>15,21</sup> Hence, we understand only reducing particle size of nano-Si is not the answer. Due to the buckled honeycomb structure of silicene,<sup>22–25</sup> diffusion should be enhanced drastically compared to nano-Si particles. Silicene additionally showcases some unique properties including: (a) beneficial mechanical and electronic properties;<sup>26,27</sup> (b) zero-band gap,<sup>28</sup> and (c) high influence on the future electronic industry.<sup>29</sup>

Lastly, silicene is easier to manufacture compared to oxide-free nano-Si.<sup>22–25</sup> However, experimental measurements show that there exists a strong hybridization between Si and a given substrate (such as Ag(111)<sup>30</sup>) that influences the monolayer silicene heavily. This influence can be reduced by using multilayer silicene (starting from bilayer) where stronger inter-silicene layer coupling overrides the silicene–substrate interaction.<sup>22,31</sup> In short, bilayer silicene showcases enhanced stability. Fortunately, synthesis of stabilized bilayer silicene has been

successfully seen on CaF<sub>2</sub> substrate.<sup>32</sup> Bilayer silicene anode (BSA) has already been extensively researched for LIBs using molecular dynamics (MD) simulation and shows favourable reversible reactions.<sup>33–35</sup> The current research has focused on investigating bilayer silicene with ABAB stacking as an anode material for storing Mg.

One of the key factors in determining the storing capability will be investigating diffusion and bond formation of Mg<sup>2+</sup> ion in the anode. To that end, this research introduces external E-field to simulate the charging process of MIBs and study the effect on ion diffusion.<sup>33,36,37</sup> A singular Mg<sup>2+</sup> ion was introduced into BSA and calculations of mean square displacement (MSD), interaction energy, and accurate trajectory through the anode were carried out to assess the feasibility of Mg storage in this unique anode structure.

## 2 Methods

### 2.1 Molecular dynamics simulation

In the current experiment, a bilayer silicene with  $4 \times 4$  phase was created using experimentally validated lattice parameters.<sup>35,38–40</sup> This bilayer was constructed by placing two monolayer silicene unit cells shown in Fig. 1(a) on top of each-other in ABAB stacking.

The final BSA structure shown in Fig. 1(b) has a total of 576 Si atoms in the system. At  $t = 0$ , the distance of the wall from Si atoms is set to a minimum value of 5 Å (in x and y directions), while the distance from the Si atoms of the upper sheet of silicene to the upper and lower walls of the container were set to be 11.5 Å and 5 Å respectively.<sup>34</sup> Fig. 1(e) represents the simulation box after the inclusion of vacuum.

It is important to enumerate here that this study follows a methodology of  $4 \times 4$  surface construction – a process that is validated through experimental studies of silicene grown on Ag substrate<sup>41,42</sup> – and which is distinctly different from the more theoretical free standing silicene structure. Published literature<sup>23,41,42</sup> often have conflicting information, as well as being minimal in content, on the surface configuration of the second layer of silicene. In this study, both layers were made in the  $4 \times 4$  phase, which were then energy minimized to get a more stable configuration. Furthermore, Ag substrate does not undergo chemical reaction with ions while inter-silicene layer coupling overrides the effect of substrate layers on silicene.<sup>22,31</sup> This study therefore eliminates simulating the substrate and uses a wall potential to account for the structural effect in accordance with standard practice.<sup>33,43,44</sup> This final unit cell, shown in Fig. 2, closely resembles the unit cell grown on Ag(111) substrate under ultrahigh vacuum (UHV) chamber.<sup>23,45</sup> Details on energy minimization process is provided in the latter part of the Methodology section.

The current work on bilayer silicene utilizes the EDIP (Environment Dependent Interatomic Potential)<sup>46</sup> force field. Here the energy of the configuration is expressed as a sum over single-atom energy,

$$E_i = \sum_{j \neq i} V_2(R_{ij}, Z_i) + \sum_{j \neq i} \sum_{k \neq i, k > j} V_3(\vec{R}_{ij}, \vec{R}_{ik}, Z_i)$$



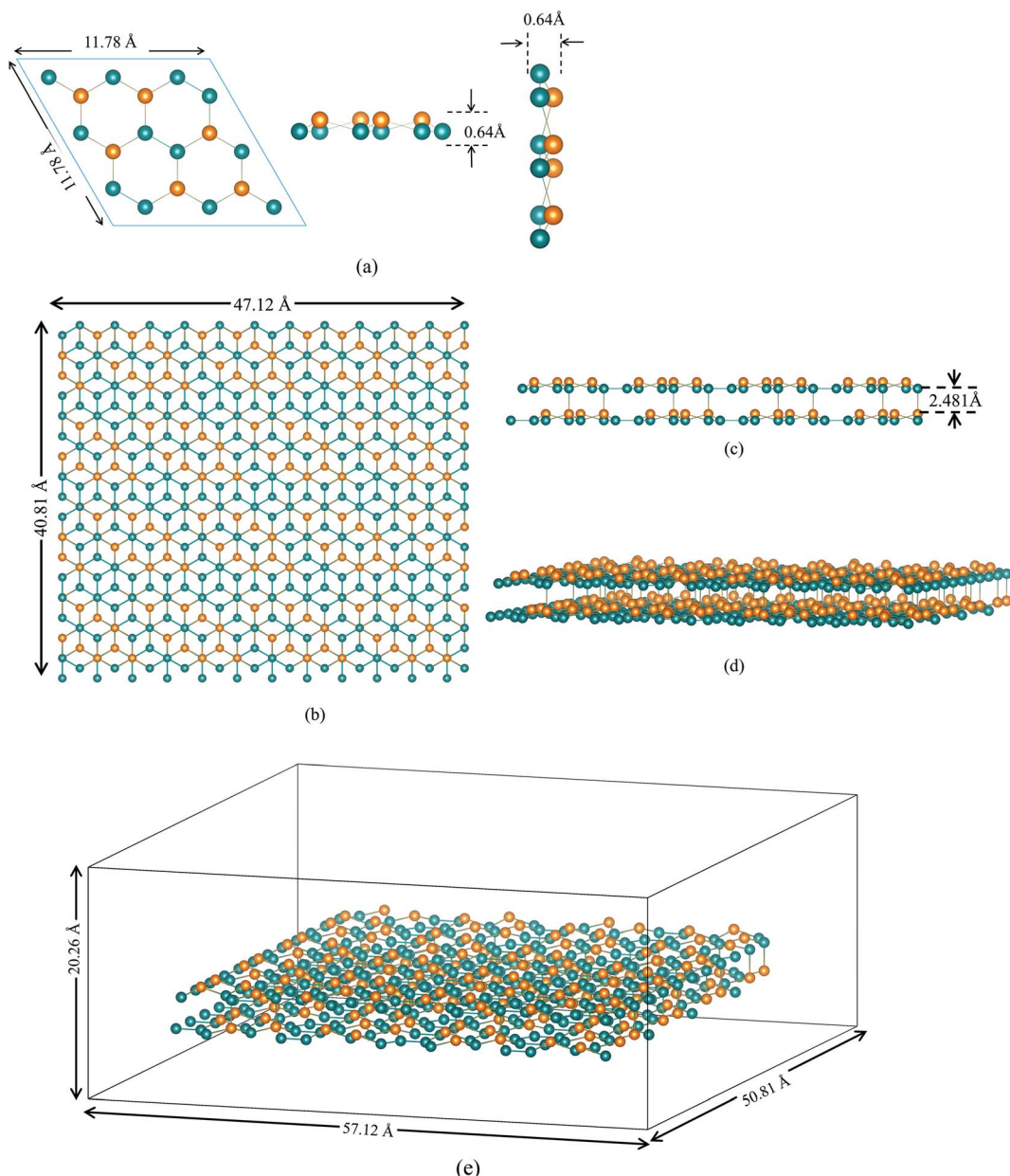


Fig. 1 (a) Silicene unit cell of layer A (top, front & side view), green-bottom Si atom, orange-top Si atom. (b) Bilayer silicene (4 × 4) surface reconstruction: top view (b), (c) side view (d) simulation model of bilayer silicene anode with applied vacuum in all three directions. (e) Simulation box after the vacuum has been included.

where the two-body  $V_2(r, Z)$  term includes repulsive and attractive interactions:

$$V_2(r, Z) = A \left[ \left( \frac{B}{r} \right)^\rho - p(Z) \right] \exp \left( \frac{\sigma}{r - a} \right)$$

$$p(Z) = e^{-\beta Z^2}$$

And the three-body term  $V_3(\vec{R}_{ij}, \vec{R}_{ik}, Z_i)$  represents radial and angular factors.<sup>46</sup> There are 13 empirical parameters in EDIP potential, and they are provided in Table 1.

Previously this potential parameters have been used in accurately calculating Young's modulus,<sup>47</sup> mechanical,<sup>48</sup> thermal transport in silicene.<sup>49</sup> With regards to simulating the interactions between Mg–Si and Mg–Mg, the current research utilized a modified Morse potential<sup>50</sup> – a choice validated by previous work as being accurate for this function. Periodic boundary conditions (PBC) were applied along all three dimensions ( $x$ ,  $y$ ,  $z$ ). To avoid the rotation of the 2D anode a weakly attractive Lennard-Jones (LJ) potential (12-6) was applied on all 6 walls of the simulation cell. Parameters of Morse & LJ potential for different interactions are given in Table 2.

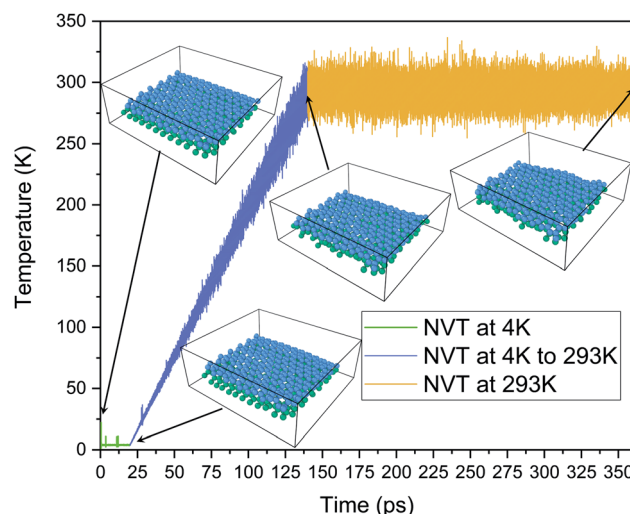


Fig. 2 Temperature evolution and corresponding minimized structures as a function of time.

Table 1 Parameters describing EDIP potential<sup>46</sup>

Parameter	Value	Parameter	Value
<i>A</i>	7.9821730 eV	$\gamma$	1.1247945 Å <sup>-1</sup>
<i>B</i>	1.5075463 Å <sup>-1</sup>	$\lambda$	1.4533108 eV
<i>a</i> (cutoff)	3.1213820 Å	$\mu$	0.6966326
<i>c</i> (cutoff)	2.5609104 Å	$\rho$	1.2085196
$\alpha$	3.1083847	$\sigma$	0.5774108 Å
$\beta$	0.0070975	$Q_0$	312.1341346
$\eta$	0.2523244		

Geometric minimization of potential energy was performed in our structure followed by a dynamic relaxation with 0.0001 ps timestep. The first step in this process was to eliminate any remaining hot spots; to that end, the structure was equilibrated under 4 K temperature for 20 ps using NVT ensemble.<sup>51</sup> The structure was then slowly heated from 4 K to 293 K under NVT ensemble over 120 ps with a heating rate of 2.41 K ps<sup>-1</sup>. Finally, another equilibration under NVT ensemble for 220 ps was run at 293 K.

We applied a considerably larger E-field (0.2 V Å<sup>-1</sup>, 0.4 V Å<sup>-1</sup>, 0.6 V Å<sup>-1</sup>, 0.8 V Å<sup>-1</sup>, 1.0 V Å<sup>-1</sup>) compared to what is applied in a commercial setting. This was done to accelerate the intercalation process in an effort to complete the computation in a reasonable time; this procedure and the range of E-field utilized are standard methods in MD simulation and have been published extensively before where the E-field range falls

typically in the 0 V Å<sup>-1</sup> to 1.5 V Å<sup>-1</sup> range.<sup>36,52-56</sup> Hence the simulation times used in this work and the experimental times in commercial batteries should not be compared directly as they are measured in different scales.

While applying external E-fields in MD simulation, an unmodified thermostat can generate faulty results due to interference. In a previous study, a modified Nose–Hoover (NH) thermostat and a CSVR thermostat which use non-Hamiltonian and Hamiltonian dynamics, respectively, were employed to account for this interference.<sup>55</sup> In the present simulation, three thermostats were employed to run MD simulation under the same E-field strength to check the consistency of the results: (a) “Nose–Hoover” ensemble (NVT) (results included in ESI†);<sup>51</sup> (b) modified “Nose–Hoover” ensemble (NVT) (results included in ESI†) where the thermostat only calculates temperature based upon kinetic energy-resolved in directions normal to the E-field;<sup>57</sup> (c) CSVR thermostat<sup>58</sup> with a separate time integrator, NVE. With high congruence in results between the three thermostat modes providing further validation of the accuracy of the executed methodology, this current work has focused on results derived using the CSVR thermostat, as it has been shown to be the least likely to manifest the “flying ice cube effect”<sup>59</sup> (ESI 1.1†) or develop problematic results due to interaction with E-field.<sup>55</sup> The quantitative details supporting these procedures have been included in the ESI file.†

The large-scale atomic/molecular massively parallel simulator (LAMMPS)<sup>60</sup> program developed by Plimpton *et al.* was utilized to perform simulations to calculate relevant properties and predict the behavior of the Mg<sup>2+</sup> ion in the BSA channel. The Verlet algorithm was used to integrate Newton's equations of motion. A very small timestep of 0.00001 ps or 0.01 fs ( $1 \times 10^{-17}$  s) was utilized and the simulation was run for 50 ps. A small time step of 0.01 fs was used to accurately calculate the trajectories because during velocity rescaling in MD, using larger time steps could result in larger atomic jumps in between consecutive time steps leading to a faultier trajectory. Time step values in the range of 0.01–2 fs can be seen in published literature.<sup>25,44,55,56,61-65</sup>

## 2.2 First-principle calculations

In this study, first-principle calculations were performed to further verify the validity of utilizing the EDIP potential and the modified Morse potential for capturing the physics of silicene and Si–Mg interactions respectively. To this end, Density Functional Theory (DFT) calculations were carried out within the framework of the Vienna Ab initio Software Package (VASP).<sup>66,67</sup> The approximations to the exchange–correlation

Table 2 Parameters describing various interactions

Interaction	<i>D</i> (strength of the interaction, eV)	$\alpha$ (range of the interaction, Å <sup>-1</sup> )	$r_0$ (position of the potential minimum, Å)
Mg–Si (Morse) <sup>50</sup>	0.4420	1.0572	2.7552
Mg–Mg (Morse) <sup>50</sup>	0.5404	0.7921	3.1814
Wall parameter (LJ 12-6) <sup>34,36</sup>	0.01	1	2.5



functional were computed using the Generalized Gradient Approximation (GGA)<sup>68</sup> together with the Perdew–Burke–Ernzerhof functional. The DFT-D3 method<sup>69</sup> was employed to accurately describe the van der Waals interactions. The governing Kohn–Sham equations were solved using the projector wave augmented method.<sup>70</sup> Since DFT is more computationally expensive, a smaller unit cell containing 72 Si atoms was used to model the BSA structure and for Mg-intercalation a single Mg<sup>+</sup> ion was placed within the bilayer of this silicene cell.

The ground state electronic density and corresponding ground state energies were computed using a plane-wave basis set energy cut-off of 700 eV and a  $3 \times 2 \times 1$  gamma-centered Monkhorst–Pack *K*-point grid. The lattice of the BSA was relaxed *via* the force-based conjugate gradient approach<sup>71</sup> with an energy convergence tolerance of  $10^{-8}$  eV and a force/ion tolerance of 0.02 eV Å<sup>-1</sup>. To perform validation studies, the per atomic cohesive energy of pure silicene was computed using DFT using the following equation,

$$E_{\text{cohesive}} = \frac{E_{\text{BSA}}}{N} - E_{\text{isolated silicon}}$$

where  $E_{\text{BSA}}$  is the ground state energy of the bilayer silicene anode,  $N$  is the number of atoms in the BSA unit cell and  $E_{\text{isolated silicon}}$  is the energy of a single isolated silicon atom in vacuum. These results were then compared to those computed within the framework of MD using EDIP, Tersoff and Morse potentials as shown in Table 3.

EDIP provides the closest agreement to the DFT computed cohesive energy, with Tersoff potential being a close second. On the other hand, Morse potential is very inaccurate in modeling the silicene structure as it predicts positive cohesive energy which would constitute a repulsive interaction between the silicene atoms. This validates the choice of EDIP potential as a suitable inter-atomic potential for modeling the physics of the silicene bilayer.

This study also uses a modified Morse potential to capture the Si–Mg interaction for Mg intercalation within the bilayer silicene. To demonstrate that the hybrid EDIP and modified Morse potential are sufficient in describing the Mg–silicene system, the absorption energy of Mg within BSA was computed using both MD & DFT. The following equation was employed for the calculation of absorption energy,

$$E_{\text{absorption}} = E_{\text{BSA-Mg}} - E_{\text{pristine-BSA}} - \mu_{\text{Mg}}$$

where  $E_{\text{BSA-Mg}}$  is the energy of the optimized structure of Mg absorbed in bilayer silicene,  $E_{\text{pristine-BSA}}$  is the energy of pristine bilayer silicene without Mg insertion and  $\mu_{\text{Mg}}$  is the chemical

**Table 3** Comparing cohesive energy for different pair potential with DFT

Cohesive energy/atom (eV)			
DFT	EDIP <sup>46</sup>	Tersoff <sup>72</sup>	Morse <sup>50</sup>
-4.174	-4.101	-4.02	2.751

**Table 4** Comparing the adsorption energy calculated using DFT and MD method

Absorption energy (eV)	
DFT	MD
-0.111	-0.081

potential of a single Mg atom. The comparison between DFT results and those predicted by the hybrid MD potential proposed in this study is shown in Table 4.

These results validate the use of modified Morse potential in hybrid form along with EDIP to capture the physics of Mg–Si interaction in a bilayer silicene anode.

## 3 Results and discussion

### 3.1 Effect of E-field

**3.1.1 Diffusion.** In battery research, diffusion of ion in anode plays a key part in determining the suitability of the battery material. Moreover, in an MD model, it is crucial to be able to determine if a particle is deviating (in geometrical space) solely due to diffusion or if there are other factors at play. To that end, we focus of MSD calculation to shed insight into diffusion phenomenon of Mg<sup>2+</sup> ion in silicene anode. The MSD calculation is atom averaged. A vector of four quantities is calculated where the first 3 elements of the vector are the squared dx, dy, dz displacements, summed and averaged over atoms in the group:

$$\text{MSD}_x = \frac{\sum \text{dx}^2}{\text{atoms}}$$

The fourth element is the total squared displacement, *i.e.* (dx  $\times$  dx + dy  $\times$  dy + dz  $\times$  dz), summed and averaged over atoms in the group. The deviation of position for MSD calculation is taken with respect to the initial position of the Mg<sup>2+</sup> ion. Smoothed MSD vs. time curves presented in Fig. 3 demonstrate the trends clearly by eliminating minute vibrations; the unsmoothed curves can be found in the ESI section (refer to ESI: 1†).

In the present experiment, an external E-field was applied in the *x*-direction. This led, as expected, to the distinctive movement of the Mg<sup>2+</sup> ion in the *x*-direction as shown in Fig. 3(a), and with some degree of random motion observed in the *y* and *z* directions shown in Fig. 3(b) and (c) respectively. This serves as a validation of E-field being the primary contributor for the diffusion of Mg<sup>2+</sup> in BSA.

From the graph in Fig. 3(a), it can be observed that there is little to no changes in the Mg<sup>2+</sup> ion position in the absence of an E-field (highest value for MSD  $\sim 49 \times 10^{-20}$  m<sup>2</sup>). In the absence of E-field, diffusion of ion is solely dependent on thermal contribution and hence Fig. 3(a) indicates that the thermal contribution for the Mg<sup>2+</sup> ion displacement is very trivial. This phenomenon is better observed in Fig. 4 where the trajectory of Mg<sup>2+</sup> ion under 0 V Å<sup>-1</sup> represented by trajectory 1 shows barely any movement with time. Now, applying 0.2 V Å<sup>-1</sup> at the same



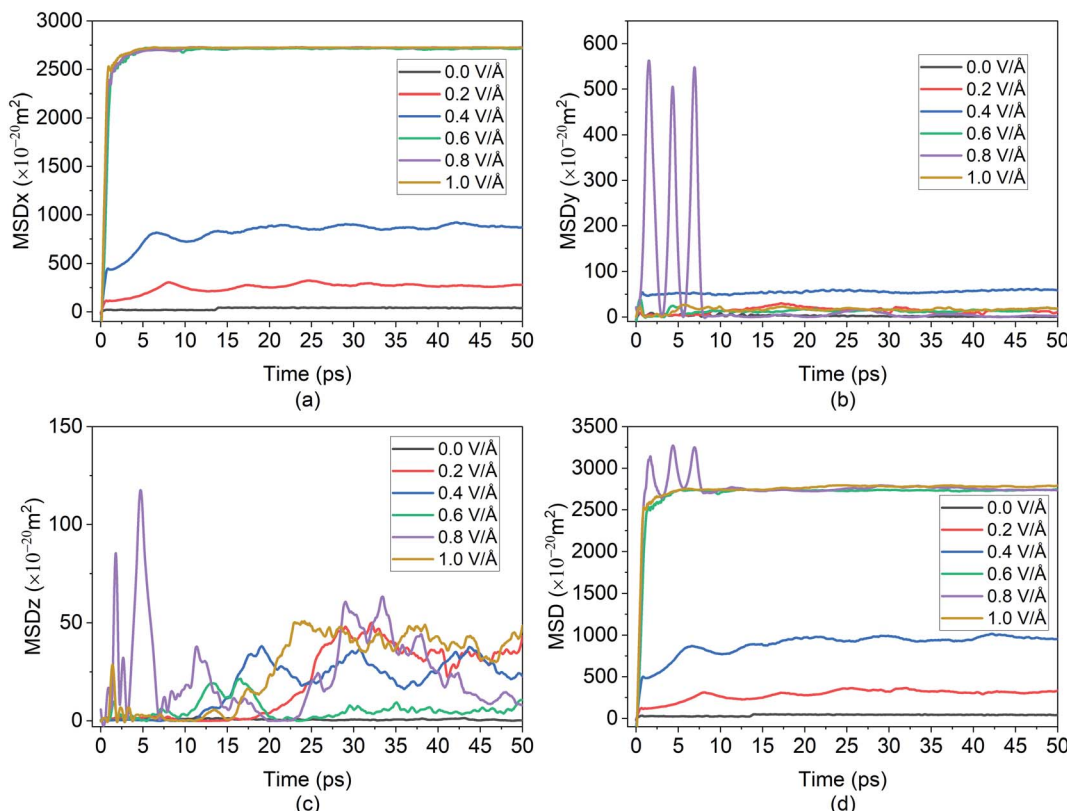


Fig. 3 Smoothed curve: (a) MSD of  $\text{Mg}^{2+}$  ion in  $x$  direction vs. time. (b) MSD behaviour in  $y$  direction vs. time, demonstrating randomness (c) MSD behaviour in  $z$  direction vs. time, demonstrating randomness. (d) Total MSD vs. time.

temperature ( $\sim 293$  K) (hence with the same thermal contribution) leads to a large jump in MSD ( $\sim 300 \times 10^{-20} \text{ m}^2$ ) and larger movement in  $x$  direction in trajectory 2 shown in Fig. 4. As can be observed from both the MSD curve in  $x$  direction and trajectory profile given in Fig. 3(a) and 4 respectively, with increasing E-field strength  $\text{Mg}^{2+}$  ion travels larger distance. The most significant impact occurs when  $0.6 \text{ V} \text{ \AA}^{-1}$  is applied – four times larger in magnitude compared to the MSD value when an E-field of  $0.4 \text{ V} \text{ \AA}^{-1}$  is applied ( $\sim 900 \times 10^{-20} \text{ m}^2$  at  $0.4 \text{ V} \text{ \AA}^{-1}$  vs.  $\sim 2710 \times 10^{-20} \text{ m}^2$  at  $0.6 \text{ V} \text{ \AA}^{-1}$ ). Moreover, we can see that prior to  $0.6 \text{ V} \text{ \AA}^{-1}$ , increase in E-field (from  $0.2 \text{ V} \text{ \AA}^{-1}$  to  $0.4 \text{ V} \text{ \AA}^{-1}$ ) results in a comparatively smaller increase in MSD – with a difference in values  $\sim 600 \times 10^{-20} \text{ m}^2$ . From Fig. 4, the trajectory profile of  $\text{Mg}^{2+}$  ion under  $0.6 \text{ V} \text{ \AA}^{-1}$  represented by trajectory 4 at both 1 ps and 50 ps shows significantly larger movement compared to trajectory 1, 2 & 3 representing  $\text{Mg}^{2+}$  movement at 0, 0.2, 0.4  $\text{V} \text{ \AA}^{-1}$  respectively. The reason becomes apparent in Fig. 4, where at a lower E-field strength, the ion can only move a few nanometres ( $< 10$  nm) of distance inside the BSA channel. On the other hand, under the influence of a higher E-field strength ( $\geq 0.6 \text{ V} \text{ \AA}^{-1}$ ), the ion reaches the end portion of the anode with ease (within 1 ps).

It can be further seen from the trajectory profile in Fig. 4 that within the first  $\sim 1$  ps, the  $\text{Mg}^{2+}$  ion under all E-field strength finds its equilibrium position, and this distance travelled is directly proportional to the E-field strength (the higher the strength, it is clearly seen that the more the distance the ion

traverses). To further prove this assertion, we provide the MSD and interaction energy curve with respect to time in Fig. 5(a) and (b) respectively, where we can see even though there are fluctuations in data prior to reaching 1 ps, the trends stabilize and show clear sign of reaching their equilibrium position. A detailed discussion on interaction energy can be found in later section.

Furthermore in Fig. 4, it can be noticed that after 50 ps of simulation, the ion is locked into a fixed  $x$ -position. The only changes in position observed are in the  $z$  direction – this can be attributed to the movement of the entire bilayer silicene in that  $z$  direction. Movement of BSA corresponds to the lack of structural support in  $z$  direction as unlike the bulk, the 2D material has vacuum surrounding it. In a real system, this movement will be limited due to anode being confined by surrounding insulating material, or neighbour 2D layers. In this present work a similar effect was simulated by applying the LJ (12-6) potential in wall in an effort to minimize and limit in the  $z$  direction. Similarly, from Fig. 6(a), it can be further observed, after the initial jump in MSD in  $x$  direction upon application of an E-field of  $0.6 \text{ V} \text{ \AA}^{-1}$ , further increase in the E-field strength does not have a noticeable impact on MSD. The dense and large oscillating MSD curves (in the top zoomed-in graph of Fig. 3(a)) are indicative of the same conclusion, interaction of the ion with the wall potential. It is noticed however that after a while, the ion demonstrates fewer oscillations and reaches a saturation level. It is known that saturation in any given MSD curve is



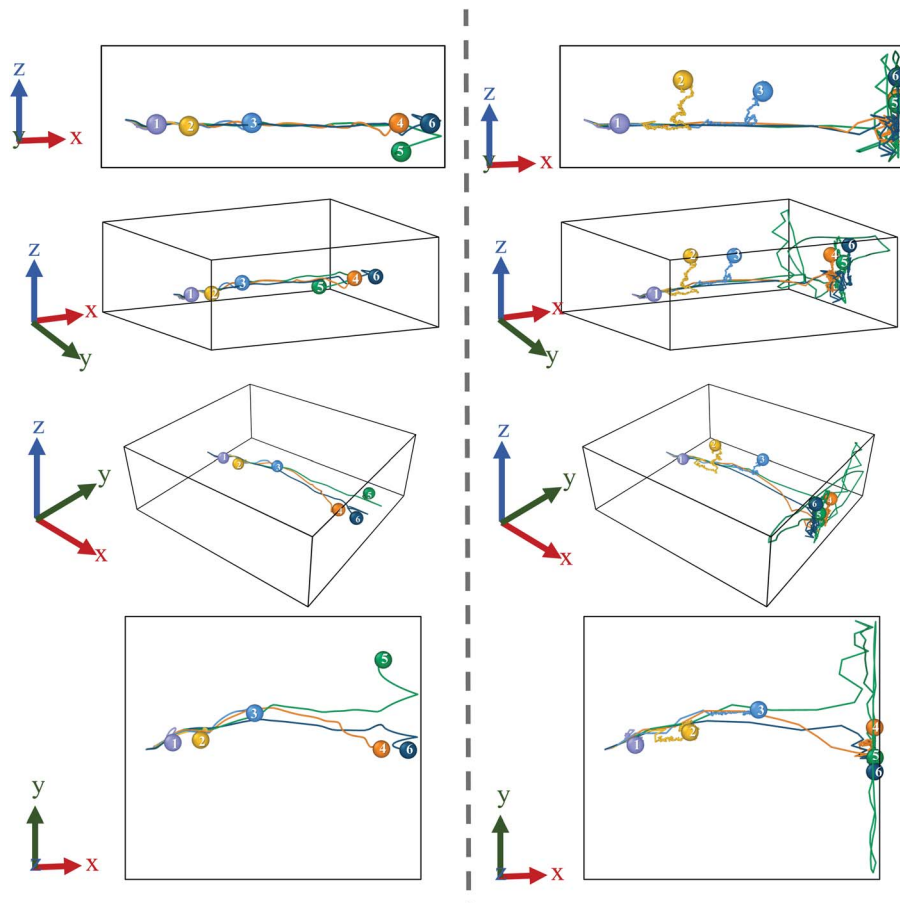


Fig. 4 Left column represents trajectory for 1 ps and right side represent 50 ps; data was taken every 0.01 ps & 0.1 ps for left and right columns, respectively. From top to bottom: front, ortho, perspective & pop view ((1) lavender-0.0 V Å⁻¹, (2) yellow-0.2 V Å⁻¹, (3) blue-0.4 V Å⁻¹, (4) orange-0.6 V Å⁻¹, (5) green-0.8 V Å⁻¹, (6) dark blue-1.0 V Å⁻¹).

characteristic of solid phase behaviour, where the ion remains in its fixed position and undergoes vibration.<sup>56</sup> It can thus be clearly stated here that the  $Mg^{2+}$  ion in the current system has formed strong bonds with the Si atoms in BSA and has thereby become locked-in within the solid matrix and the MSD shows a saturation instead of growth. This fact implies that in the

presence of a barrier, the ion can form bonds with BSA even at high E-field values.

As ion movement is primarily seen in  $x$  direction, total MSD curve shown in Fig. 3(d) naturally resembles the MSD behaviour in that direction. An interesting deviation is observed under  $0.8$  V Å⁻¹ where a significant contribution of MSD in  $y$  and  $z$  directions under  $0.8$  V Å⁻¹. This is also observed in Fig. 4, where

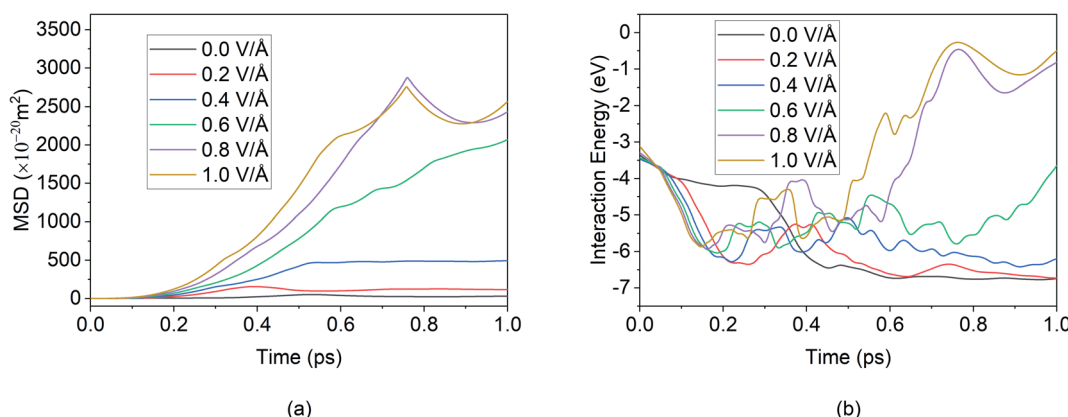


Fig. 5 Smoothed curve: (a) total MSD vs. time (b) interaction energy vs. time for first 1 ps of simulation.



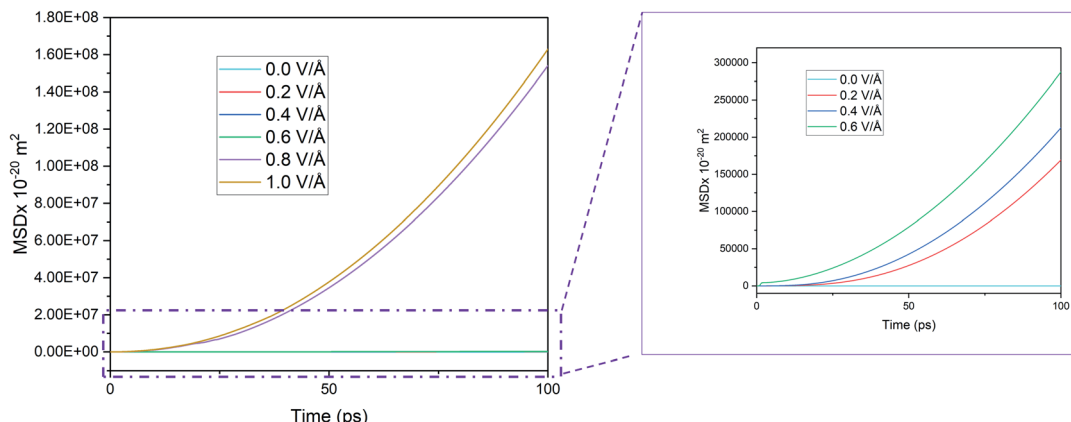


Fig. 6 MSD in x direction of  $Mg^{2+}$  ion in BSA for 100 ps in the absence of applied boundary condition.

comparing trajectory 5 & 6 representing  $Mg^{2+}$  ion movement under  $0.8 \text{ V } \text{\AA}^{-1}$  and  $1.0 \text{ V } \text{\AA}^{-1}$  we can notice a significant movement is seen in  $y$  as well as  $z$  directions *i.e.*, highest overall random motion in trajectory 5. This behaviour does not correspond to the movement of entire BSA; rather, it is an effect of the free movement of the  $Mg^{2+}$  ion after it leaves the channel and the E-field is not strong enough to keep the ion motion confined in the direction of field ( $x$  direction). However, after  $\sim 10$  ps when  $Mg^{2+}$  ion loses its momentum and come close to BSA, it finally forms bond and becomes locked in an equilibrium position as well.

While a consistent expectation would be that  $1 \text{ V } \text{\AA}^{-1}$  producing trajectory 6 showcases a similar, if not higher

randomness, compared to trajectory 5, the results show an opposite behaviour. A logical hypothesis for this phenomenon could be that a higher E-field ( $1 \text{ V } \text{\AA}^{-1}$ ) overrides the randomness of the  $Mg^{2+}$  ion, forcing it to move primarily in the  $x$  direction, and to ultimately face restrictions only on the face of boundary. This is further validated as the largest  $x$ -direction displacement is observed under  $1 \text{ V } \text{\AA}^{-1}$  and can be seen in trajectory (Fig. 4) and MSD in  $x$  direction (Fig. 3(a)). It therefore appears that an E-field of  $0.8 \text{ V } \text{\AA}^{-1}$ , showcasing trajectory 5, is an inflection point in the spatial behaviour of the  $Mg^{2+}$  within the BSA.

Now, as mentioned earlier, at higher E-field ( $\geq 0.6 \text{ V } \text{\AA}^{-1}$ ) and below  $\sim 1$  ps, the ion leaves the BSA channel; it can therefore be

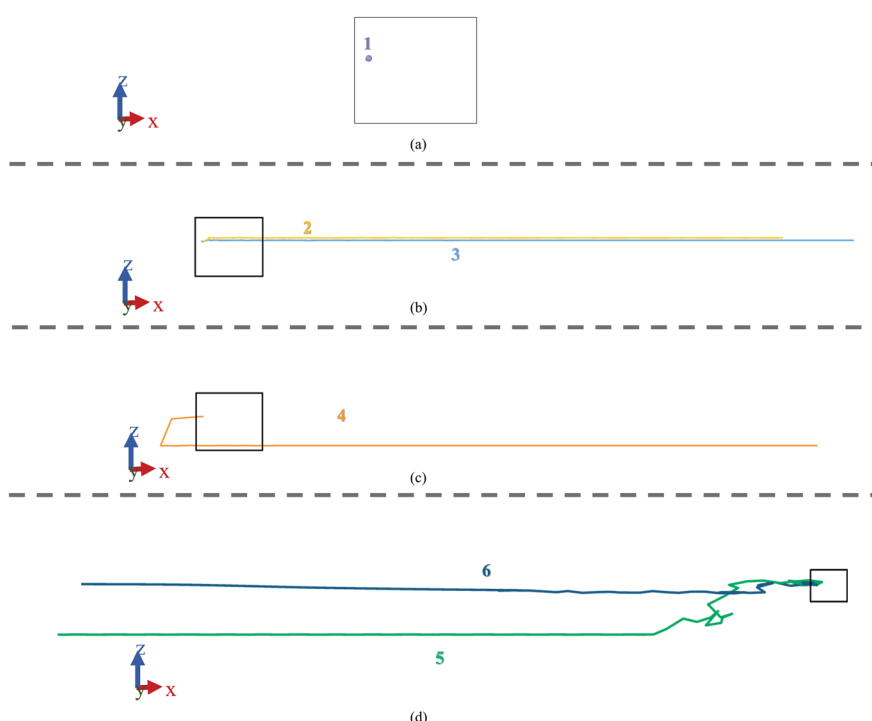


Fig. 7 Trajectory for 100 ps in the absence of boundary condition; data was taken every 5 ps. From top to bottom trajectories: (a) under  $0.0 \text{ V } \text{\AA}^{-1}$  (b) under  $0.2 \text{ V } \text{\AA}^{-1}$  &  $0.4 \text{ V } \text{\AA}^{-1}$  (c) under  $0.6 \text{ V } \text{\AA}^{-1}$  (d) under  $0.8 \text{ V } \text{\AA}^{-1}$  &  $1.0 \text{ V } \text{\AA}^{-1}$ .



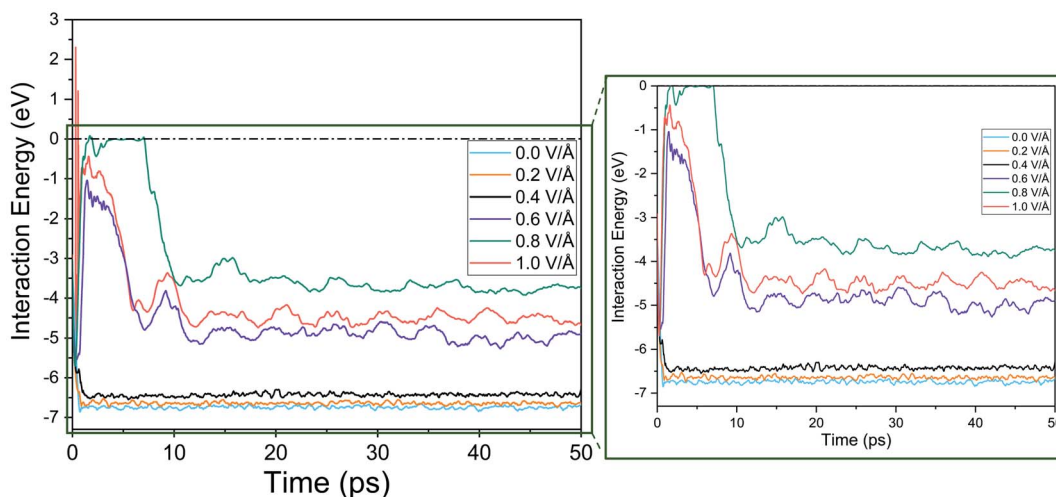


Fig. 8 Interaction energy between  $Mg^{2+}$  ion and bi-layer silicene anode with respect to increasing electric field.

extrapolated that the bond formation was largely assisted *via* the presence of boundary. In a real-life situation, for a battery under a larger charging voltage together with complex interactions between several ions present in the system, the interaction between boundary and individual ions might be much more complicated.

Given this context, we removed the vacuum in the  $x$  and  $y$  directions and removed the wall potentials and then ran the simulation for 100 ps under periodic boundary condition. In the absence of the applied boundary condition the changes in MSD curve in  $x$  direction is given in Fig. 6.

Here we notice that the MSD of  $Mg^{2+}$  ion in  $x$  direction keeps on growing, in contrast to Fig. 3(a) that showed that the MSD curve in  $x$  direction stopped growing within the first few picoseconds when boundary condition was applied. However, in Fig. 6, the growth is seen even below  $0.6 \text{ V } \text{\AA}^{-1}$  where they supposedly didn't interact with wall potential previously. To investigate this phenomenon further, trajectory profile for 100 ps in absence of boundary conditions is given in Fig. 7, where

we can visualize that, this movement is actually attributed to the entire BSA movement under applied E-field in  $x$  direction, as in the absence of a boundary condition, a 2D material will have no support to hold it in place. As the trajectory profile was generated under PBC conditions (unwarped), movement of entire system (BSA &  $Mg^{2+}$  ion) is represented by lines moving forward from the simulation cell, whereas in case when movement of only ion is present, lines appear backward moving. From trajectory profiles given in Fig. 7(a), we can see at  $0.0 \text{ V } \text{\AA}^{-1}$  there's no movement in the system. In Fig. 7(b), we notice trajectory 2 & 3 under E-field strength  $0.2 \text{ V } \text{\AA}^{-1}$  and  $0.4 \text{ V } \text{\AA}^{-1}$  respectively, the entire system moves towards the E-field. As BSA is charge neutral, movement of BSA only occurs when it forms strong bonds with cation  $Mg^{2+}$ . We also notice trajectory 3 is greater than trajectory 2. We see an interesting phenomenon for trajectory 4 given in Fig. 7(c) under E-field strength  $0.6 \text{ V } \text{\AA}^{-1}$ , at first trajectory moves backwards for first  $\sim 18.56$  ps, signifying  $Mg^{2+}$  ion doesn't form any bonds during this period. After this initial random movement,  $Mg^{2+}$  ion indeed finds an

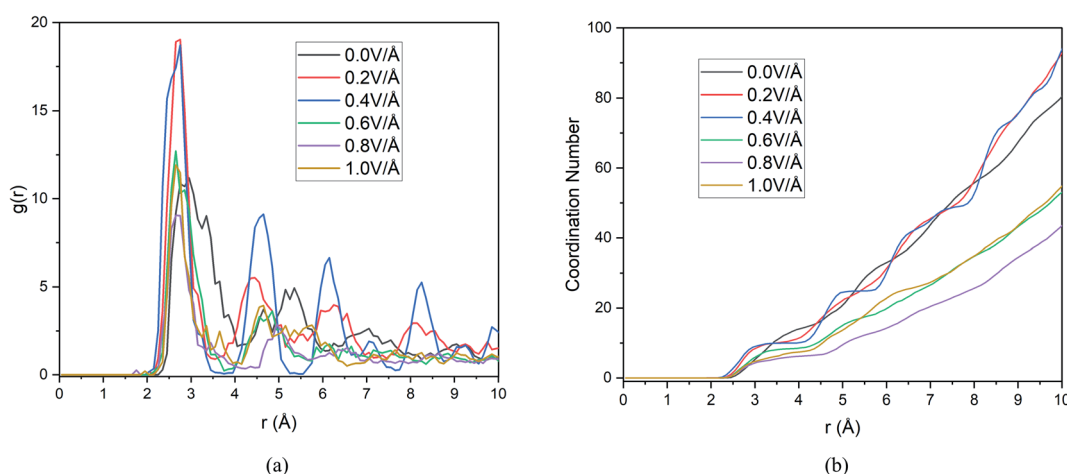


Fig. 9 Changes in (a) RDF analysis & (b) coordination number (CN) under the effect of different electric field.

Table 5 Validation of bond-length &amp; summarized coordination number for nearest neighbour shell

Data source	Mg–Si bond length (Å)	
Experimental <sup>73</sup>	2.664, 2.733, 2.861	
First-principal calculation	2.7552 (ref. 50) 2.77 (ref. 74)	
Simulation	E-field strength	
	Bond length (Å)	
	Coordination number (nearest neighbour shell around $Mg^{2+}$ ion)	
0.0 V Å <sup>-1</sup>	2.95	8.0396
0.2 V Å <sup>-1</sup>	2.75	10.08911
0.4 V Å <sup>-1</sup>	2.75	9.9703
0.6 V Å <sup>-1</sup>	2.65	8.33663
0.8 V Å <sup>-1</sup>	2.65	5.09901
1.0 V Å <sup>-1</sup>	2.65	5.51485

equilibrium position and form bonds; hence trajectory 4 shows forward movement for the rest of the simulation period. A stark contrast is observed at Fig. 7(d) where trajectory 5 and 6 under the E-field value of  $0.8 \text{ V Å}^{-1}$  and  $1.0 \text{ V Å}^{-1}$  shows only backward movement, signifying ions don't form bonds in the system. MSD curve in Fig. 6 also shows that at  $E\text{-field} \geq 0.8 \text{ V Å}^{-1}$ , the MSD curve grows significantly more than that is observed under  $0.6 \text{ V Å}^{-1}$ , which signifies higher diffusion rate of  $Mg^{2+}$  ion, which makes it harder to form bonds.

In consistent with our previous observation of  $0.8 \text{ V Å}^{-1}$  being the inflexion point of spatial movement, here as well we notice higher random movement for trajectory 5 compared with rest including trajectory 6.

### 3.2 Interaction energy

The interaction energy is the total energy of interactions between  $Mg^{2+}$  ion with all the Si atoms in BSA based on the pair potentials acting between these two species. Thus, the computed interaction energy plots represent the total energies of interaction between a single Mg and surrounding silicon atoms as it travels through the channel. Further proof of the presence of an inflection point and dependence of E-field strength on  $Mg^{2+}$  ion diffusion in BSA can be observed from the interaction energy graph given in Fig. 8, where interaction energy of the  $Mg^{2+}$  ion with silicene depends directly on the position of the ion inside the BSA channel or beyond it.<sup>33</sup> This energy therefore indirectly depends on the E-field strength

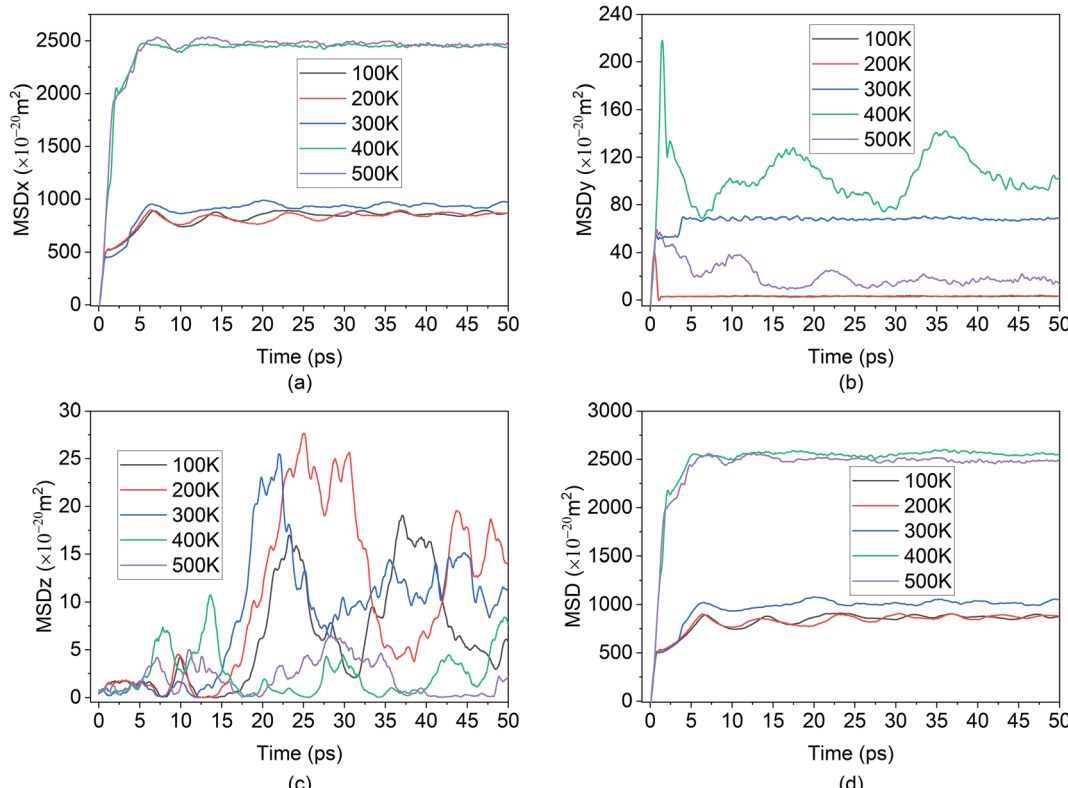


Fig. 10 Smoothed curve: (a) MSD of  $Mg^{2+}$  ion in x direction vs. time. (b) MSD behaviour in y direction vs. time, demonstrating randomness (c) MSD behaviour in z direction vs. time, demonstrating randomness. (d) Total MSD vs. time for different temperature.



determining the motion of the ion in the channel. Naturally at higher E-field, ion motion will be higher and hence more interaction energy will be expected which proves right for E-field values 0.0–0.6 V  $\text{\AA}^{-1}$ , as can be observed in Fig. 8.

It is noticed that interaction energy is higher at an E-field strength of 0.8 V  $\text{\AA}^{-1}$  compared to that at 1 V  $\text{\AA}^{-1}$ . As discussed previously, after 0.8 V  $\text{\AA}^{-1}$ , the  $\text{Mg}^{2+}$  ion leaves the anode easily and shows random motion in  $y$  and  $z$  direction. Again, while it is a reasonable expectation that at 1 V  $\text{\AA}^{-1}$  similar, if not higher, randomness and MSD in  $y$ ,  $z$  would be observed, the reality does not show that. This is because a higher E-field beyond the critical inflection point of 0.8 V  $\text{\AA}^{-1}$  overrides the randomness of the  $\text{Mg}^{2+}$  ion, leading to its movement primarily in the  $x$  direction, leading ultimately for it to face restrictions on the face of the wall boundary.

At 0.8 V  $\text{\AA}^{-1}$ , prior to 10 ps, 0 eV energy between  $\text{Mg}^{2+}$  and silicene is observed. This indicates that during this time period, the  $\text{Mg}^{2+}$  ion leaves the BSA channel and moves randomly till coming close enough again to start interacting with silicene and forming bonds. Similar phenomenon is also noticeable for 0.6 V  $\text{\AA}^{-1}$  and 1 V  $\text{\AA}^{-1}$  but with less severity (prior to 10 ps, and with the energy never reaching 0 eV). At 0.6 V  $\text{\AA}^{-1}$ , the ion leaves the channel and returns instantaneously as the provided E-field is

not enough to propel it further; at 1 V  $\text{\AA}^{-1}$ , only movement is seen at  $x$  direction where bonds between Mg–Si are formed.

### 3.3 Radial distribution function (RDF)

For successful intercalation of ion, it not only needs to have easy diffusion capability in anode but also the ability to form bond and stay bonded for a required period of time (during charging). Finally, after adequate analysis on diffusivity of  $\text{Mg}^{2+}$  ion, we need to focus on bond formation of ion in anode, to that end we provide RDF analysis which will reveal the probability of finding a given particle at a distance from another tagged particle. In this section we include RDF analysis under applied boundary condition, as boundary conditions doesn't alter RDF much due to the analysis being limited to mostly the nearest neighbour shells. The RDF analysis in Fig. 9(a), reveals distribution of Si atoms around  $\text{Mg}^{2+}$  ion and the first major peak indicates the nearest neighbour (NN) distances from central atom ( $\text{Mg}^{2+}$  ion).

These results and the CN numbers of first NN shell is summarized in Table 5, which reveals that NN bond distance decreases with increasing E-field. The calculated bond distance under E-field application 2.75  $\text{\AA}$  is closely comparable to experimental<sup>73</sup> and first principal calculation,<sup>50,73,74</sup> this serves

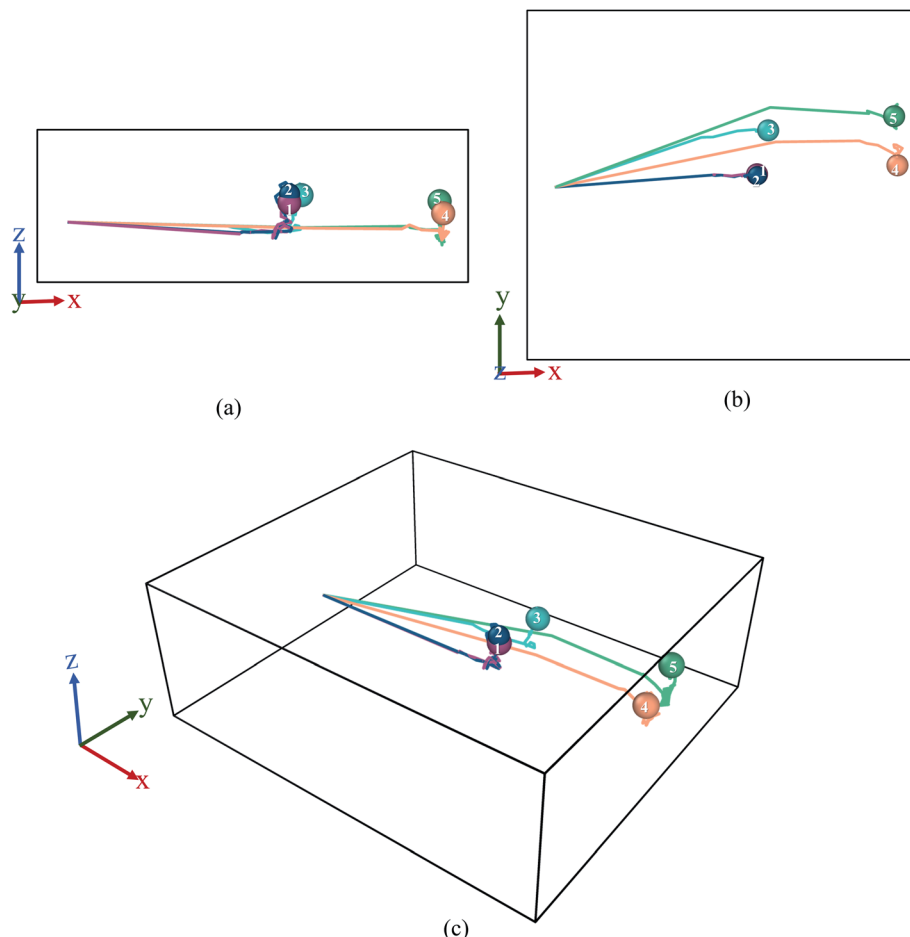


Fig. 11 Trajectory profile for 50 ps where data was taken every 0.1 ps. Here, (a) front, (b) top, (c) perspective view ((1) purple-100 K, (2) blue-200 K, (3) sky blue-300 K, (4) orange-400 K, (5) green-500 K).



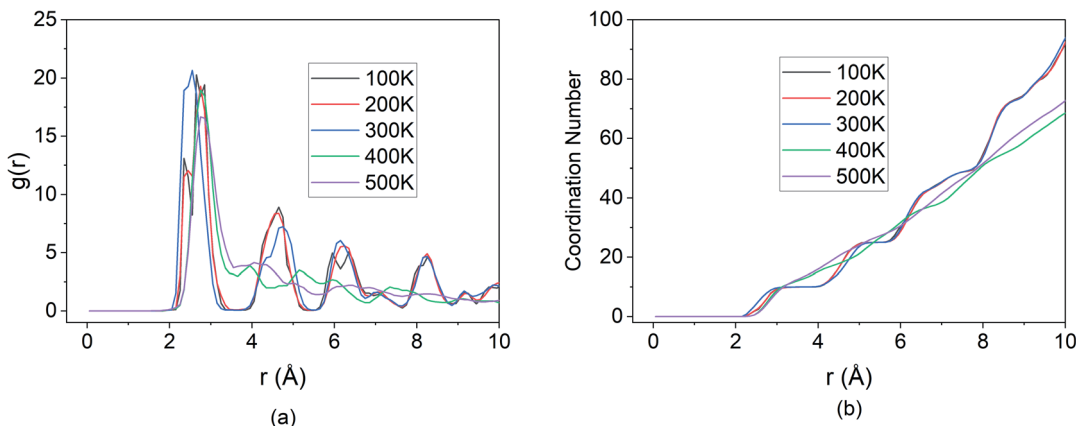


Fig. 12 Changes in (a) RDF analysis & (b) coordination number (CN) under the effect of different temperature.

as a validation step for our current result. However, we notice the highest probability of finding NN atoms is observed under 0.2 & 0.4 V  $\text{\AA}^{-1}$  and further increase in E-field decreases the probability drastically. We also notice that  $\leq 0.4$  V  $\text{\AA}^{-1}$  peaks seen in Fig. 9(a) is much more ordered that is indicative of solid phase.

Now, in Fig. 9(b) we include the coordination number as a function of cut off distance. In consistent with RDF analysis, we observe highest growth of CN at 0.2 & 0.4 V  $\text{\AA}^{-1}$ , increasing the E-field any further decreases CN to a lower value than that of CN at

0.0 V  $\text{\AA}^{-1}$ . As we know, higher CN value indicates higher chance of bond formation, as  $\text{Mg}^{2+}$  ion will be surrounded by more Si atom in its NN shell. Hence bond formation is highest at the E-field range of 0.0–0.4 V  $\text{\AA}^{-1}$ . Therefore, we conclude that, even though diffusion increases at higher E-field strength, bond formation doesn't take place beyond 0.4 V  $\text{\AA}^{-1}$ . On the other hand, even though in the absence of E-field, bond formation takes place as can be seen from RDF graph, we notice from Section 3.1.1, diffusion doesn't take place in the absence of E-field for any boundary condition. This indicates that there exist an

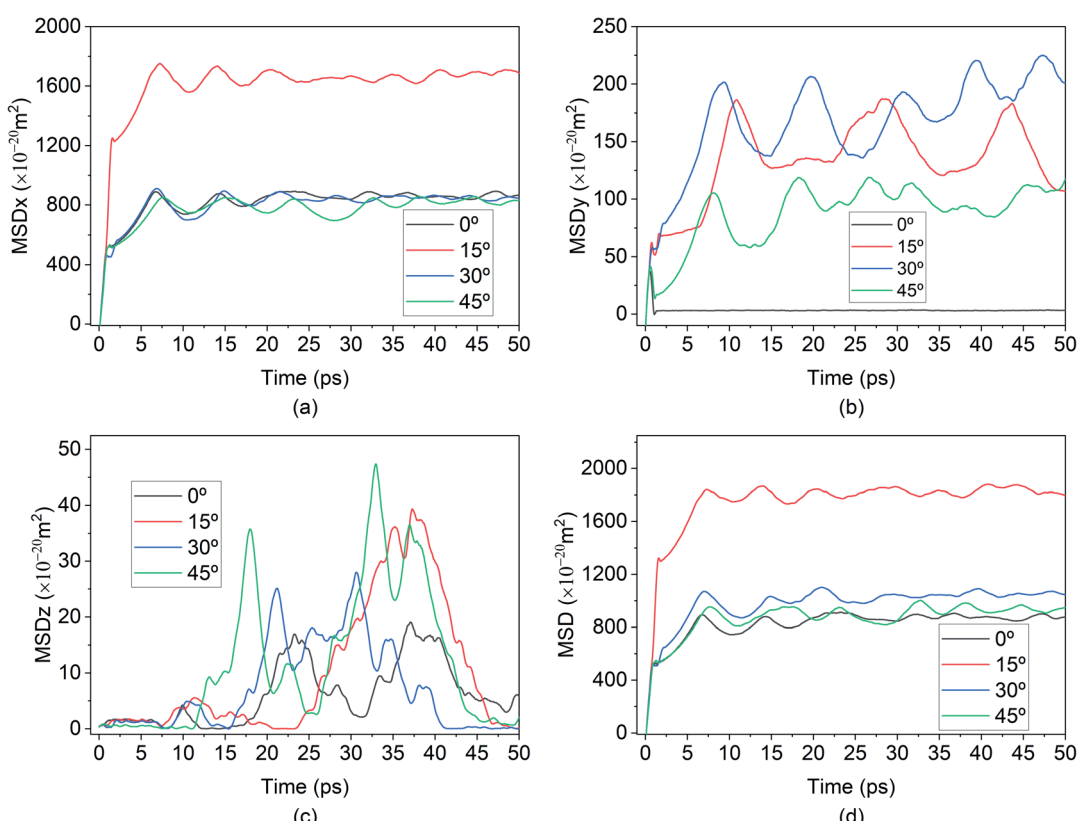


Fig. 13 Smoothed curve: (a) MSD of  $\text{Mg}^{2+}$  ion in x direction vs. time. (b) MSD behaviour in y direction vs. time, demonstrating randomness (c) MSD behaviour in z direction vs. time, demonstrating randomness. (d) Total MSD vs. time for different direction of E-field application.



optimum E-field range, in our case 0.2–0.4 V Å<sup>-1</sup>, where E-field is strong enough to ensure diffusion as seen in Section 3.1.1 and weak enough to ensure bond formation with highest CN numbers. This synergy between diffusion and bond formation, will play an important role in defining E-field parameter, even in experimental setup to ensure the intercalation of Mg<sup>2+</sup> ion in BSA.

### 3.4 Effect of temperature

The effect of temperature on the Mg intercalation in the BSA was investigated by running the same simulation set-up at temperatures of 100 K, 200 K, 300 K, 400 K & 500 K. From the temperature-dependent MSD curves given in Fig. 10, it is clear that there exists an inflection point between 300 K & 400 K where the extent of diffusion is greatly increased. There is a clear jump in the total MSD for temperatures of 400 K & 500 K ( $\sim 2500 \times 10^{-20} \text{ m}^2$ ) relative to the total MSD at the lower temperatures of 100 K, 200 K & 300 K ( $\sim 1000 \times 10^{-20} \text{ m}^2$ ). Similar to the previous section, the contribution to the total MSD is dominated by the MSD in the *x*-direction, which is to be expected since the E-field was applied in that direction. The saturation of all five of the curves seems to indicate that Mg–Si

coordination and bond formation took place in all five cases, however, the trajectories paint a different picture.

It can be seen from Fig. 11, that for the higher temperatures 400 K & 500 K, the Mg-ions reached the edge of the BSA simulation cell and was only stopped due to interaction with the wall potential. Thus, successful intercalation did not take place.

This is further corroborated by the RDF shown in Fig. 12. For the temperature values of 100 K, 200 K & 300 K, the peaks of the RDF overlap indicating the same coordination number and extent of bond formation between Si and Mg for these temperatures.

However, beyond the inflection point, for temperature values of 400 K & 500 K, only the first peak of the RDF is well defined. The subsequent peaks that were present in the lower temperatures are no longer visible at higher temperatures. The first peak results from the boundary condition imposed on the wall and is representative of the Mg-ion interacting with the wall potential. However, due to the absence of Si atoms beyond the boundary, the coordination with other nearest neighbour atoms does not take place. This indicates that for the BSA structure, operating at temperatures higher than 300 K, causes the diffusion rates to

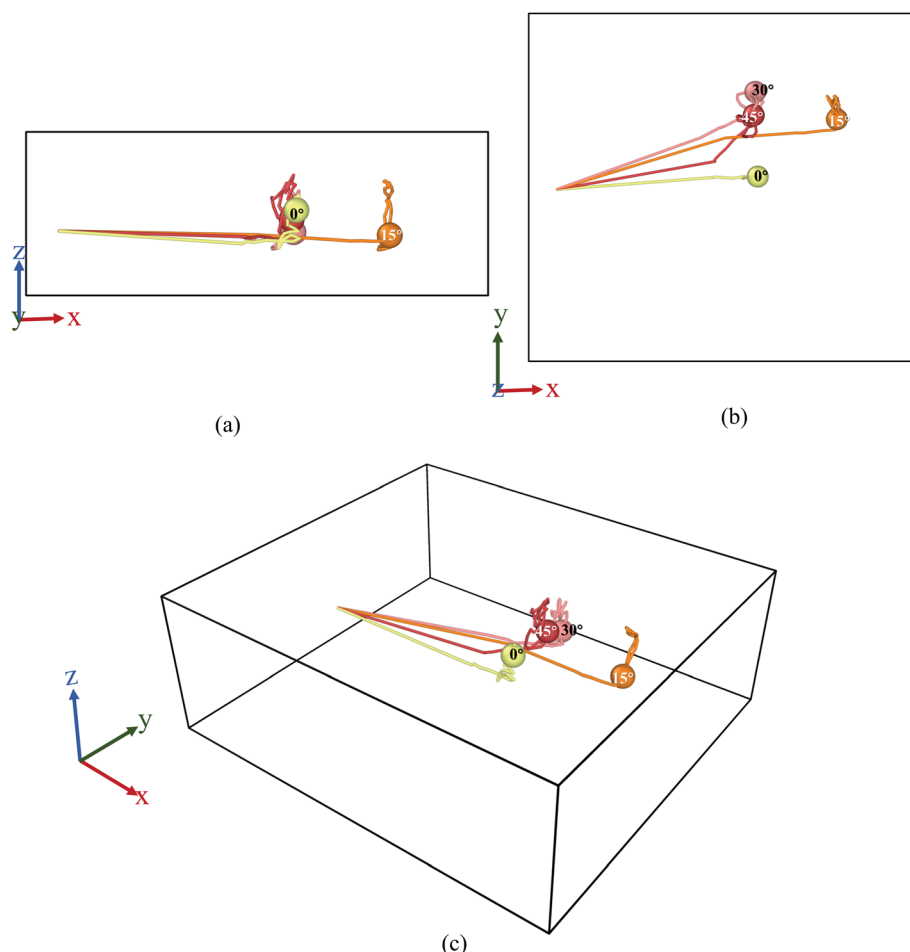


Fig. 14 Trajectory profile for 50 ps where data was taken every 0.1 ps. Here, (a) front, (b) top, (c) perspective view ((1) yellow-0°, (2) orange-15°, (3) pink-30°, (4) red-45°).



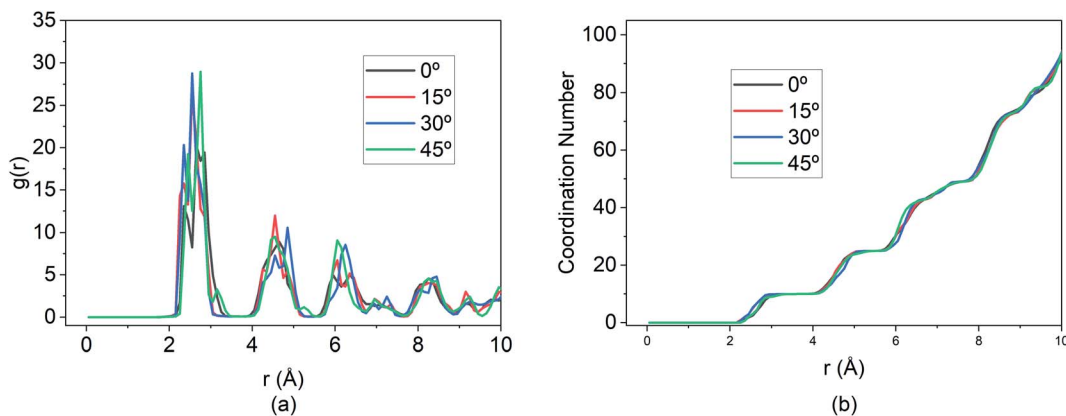


Fig. 15 Changes in (a) RDF analysis & (b) coordination number (CN) under the effect of different direction of E-field.

increase beyond the threshold at which bond formation between Si and Mg can slow down Mg diffusion. Thus, the maximum operating temperature for the simulated BSA cell exists in the 300–400 K temperature range.

### 3.5 Effect of E-field directions

The behaviours of the Mg-ion within the BSA channel doesn't only depend on the magnitude of the E-field but also on the direction in which it is applied. This direction dependency can be investigated within the framework of our MD study. Since this study is focused on the motion of the Mg-ion through the channel, the variations of the E-field will have to remain confined to the  $X$ - $Y$  plane. To illustrate how the behaviour Mg-interaction changes with the E-field direction,  $0.4 \text{ V Å}^{-1}$  E-fields were applied at respectively  $0^\circ$ ,  $15^\circ$ ,  $30^\circ$  &  $45^\circ$  from the positive  $X$ -axis in the  $X$ - $Y$  plane at a constant 100 K temperature.

As discussed before, the saturation behaviour of the MSD curve illustrated on Fig. 13, denotes the bond formation between Mg–Si within the BSA. It is therefore clear from Fig. 13(d), which denotes the total MSD behaviour of Mg-ion with respect to time and E-field direction, that the most optimal direction for Mg-ion transport within the channel is  $15^\circ$  with respect to the positive- $X$  direction. This is inferred from the higher MSD value ( $\sim 1800 \times 10^{-20} \text{ m}^2$ ) at which saturation is achieved for Mg-ions traveling at  $15^\circ$ , relative to the other three directions as shown in Fig. 13(d). This contribution to the total MSD is mainly dominated by the increase in the MSD in the  $X$ -axis. Therefore, even though the MSD in the  $Y$ -axis is largest for E-field in the  $30^\circ$  direction ( $\sim 175 \times 10^{-20} \text{ m}^2$ ), it is only slightly larger than that for the E-field in the  $15^\circ$  direction ( $\sim 150 \times 10^{-20} \text{ m}^2$ ). However, in the  $x$ -axis, the MSD in the  $15^\circ$  ( $\sim 1600 \times 10^{-20} \text{ m}^2$ ) is significantly higher compared to the  $0^\circ$ ,  $30^\circ$  &  $45^\circ$  directions. This is further confirmed by the visualization of the trajectories of the Mg atom within the BSA as shown in Fig. 14. Even though the same E-field was applied in all 4 directions, it can be clearly seen that the distance travelled by the Mg-ion in the  $15^\circ$  as indicated by the orange path, is the farthest distance relative to all other three directions. The trajectories also confirm the fact that the intercalation did take place within the BSA simulation cell and that the saturation in the MSD curves

was not brought on by the Mg-ion hitting the wall potential at the edge of the simulation box.

Additionally, the RDF shown in Fig. 15 demonstrates that while the MSD and travel path for the  $15^\circ$  E-field is significantly greater than the other three directions, the extent of bond formation between the Mg and Si is not affected by altering the E-field direction.

The peaks of the first, second and so on, nearest neighbours overlap for all three directions indicating that the coordination number is the same for all four cases. This illustrates that, at optimal E-field magnitude, altering the direction of the field can enhance the diffusion of Mg within the BSA while still ensuring similar intercalation behaviour as shown by RDF and coordination number.

## 4 Conclusions

While previous research on MIBs showcase a high rate of de-intercalation (~91.7%) of Mg from nano-Si anode, the reverse process of intercalation has never been achieved, with the prime reason being attributed to large particle sizes. In this current research, it has been shown that by decreasing dimensionality in 2D porous BSA,  $\text{Mg}^{2+}$  ion can be successfully stored (intercalated). Results further show that there exists an optimum E-field strength that's strong enough to ensure diffusion of ion in BSA and weak enough to let ion form bonds. For our current simulation setup this E-field value ranges from 0.2 to  $0.4 \text{ V Å}^{-1}$ . Hence, in the development of a Si-based anode investigation should focus on E-field parameters alongside investigating particle sizes and dimensions.

$\text{Mg}^{2+}$  ion under  $0.8 \text{ V Å}^{-1}$  shows some interesting results, with the highest displacement in  $y$  and  $z$  direction as seen from MSD curves and trajectory, also shows the highest interaction energy. Our conclusion is that the ion leaves the channel readily under this high E-field same as an ion under  $1 \text{ V Å}^{-1}$ ; however, unlike  $1 \text{ V Å}^{-1}$ , this E-field strength is not strong enough to override its tendency to move randomly and hence at  $0.8 \text{ V Å}^{-1}$ , the ion moves more freely.

Additionally, for a given E-field magnitude, varying the direction of the field changes the diffusion behavior as seen from the direction dependent MSD and trajectory. It has been



demonstrated that among the range of directions between 0° and 45°, the highest diffusion is achieved in the 15° direction. However, the RDF and CN illustrated that the change in field direction did not alter the extent of Si–Mg bond formation and thus led to successful intercalation in all cases.

Furthermore, the effect of temperature has also been investigated leading to the conclusion that there is a maximum operating temperature beyond which the thermal contribution to the diffusion will prevent the bond formation and storage of Mg within the BSA. For the present simulated cell, this inflection point exists between 300 K & 400 K.

The significance of the present research has been in proving the potential of a Si based anode for MIBs that is both inexpensive and highly efficient. Moreover, the compatibility of the silicene material with currently well-established silicon-based semiconductor industry opens the door for using current commercial electrolytes and cathode materials with the demonstrated MIB system.

## Author contributions

S. Ahsan and A. R. conceptualized the project, designed the methodology, did formal analysis, investigation, visualization and wrote the paper. S. Ahsan, A. R. and M. F. N. T. validated the model, curated data and software usage. S. Ahmed supervised the project and revised the manuscript. H. A. J., S. S., S. S. N., M. T. I., A. F. I., M. R. J., M. S. I., K. M. S. provided resources. All authors reviewed the manuscript.

## Conflicts of interest

There are no conflicts to declare.

## Notes and references

- 1 A. Manthiram, *ACS Cent. Sci.*, 2017, **3**, 1063–1069.
- 2 V. Etacheri, R. Marom, R. Elazari, G. Salitra and D. Aurbach, *Energy Environ. Sci.*, 2011, **4**, 3243–3262.
- 3 H. D. Yoo, E. Markevich, G. Salitra, D. Sharon and D. Aurbach, *Mater. Today*, 2014, **17**, 110–121.
- 4 C. Vaalma, D. Buchholz, M. Weil and S. Passerini, *Nat. Rev. Mater.*, 2018, **3**, 18013.
- 5 Y. Liang, H. Dong, D. Aurbach and Y. Yao, *Nat. Energy*, 2020, **5**, 646–656.
- 6 H. D. Yoo, I. Shterenberg, Y. Gofer, G. Gershinsky, N. Pour and D. Aurbach, *Energy Environ. Sci.*, 2013, **6**, 2265–2279.
- 7 J. W. Choi and D. Aurbach, *Nat. Rev. Mater.*, 2016, **1**, 16013.
- 8 R. Attias, M. Salama, B. Hirsch, Y. Goffer and D. Aurbach, *Joule*, 2019, **3**, 27–52.
- 9 R. Mohtadi and F. Mizuno, *Beilstein J. Nanotechnol.*, 2014, **5**, 1291–1311.
- 10 H. Dong, O. Tutusaus, Y. Liang, Y. Zhang, Z. Lebens-Higgins, W. Yang, R. Mohtadi and Y. Yao, *Nat. Energy*, 2020, **5**, 1043–1050.
- 11 D. Aurbach, Z. Lu, A. Schechter, Y. Gofer, H. Gizbar, R. Turgeman, Y. Cohen, M. Moshkovich and E. Levi, *Nature*, 2000, **407**, 724–727.
- 12 D. Aurbach, I. Weissman, Y. Gofer and E. Levi, *Chem. Rec.*, 2003, **3**, 61–73.
- 13 O. I. Malyi, T. L. Tan and S. Manzhos, *J. Power Sources*, 2013, **233**, 341–345.
- 14 L. Wang, S. S. Welborn, H. Kumar, M. Li, Z. Wang, V. B. Shenoy and E. Detsi, *Adv. Energy Mater.*, 2019, **9**, 1–7.
- 15 H. Yaghoobnejad Asl, J. Fu, H. Kumar, S. S. Welborn, V. B. Shenoy and E. Detsi, *Chem. Mater.*, 2018, **30**, 1815–1824.
- 16 D. Zhang, J. Fu, Z. Wang, L. Wang, J. S. Corsi and E. Detsi, *J. Electrochem. Soc.*, 2020, **167**, 050514.
- 17 T. S. Arthur, N. Singh and M. Matsui, *Electrochem. Commun.*, 2012, **16**, 103–106.
- 18 N. Singh, T. S. Arthur, C. Ling, M. Matsui and F. Mizuno, *Chem. Commun.*, 2013, **49**, 149–151.
- 19 Y. Shao, M. Gu, X. Li, Z. Nie, P. Zuo, G. Li, T. Liu, J. Xiao, Y. Cheng, C. Wang, J. G. Zhang and J. Liu, *Nano Lett.*, 2014, **14**, 255–260.
- 20 F. Legrain and S. Manzhos, *J. Power Sources*, 2015, **274**, 65–70.
- 21 L. R. Parent, Y. Cheng, P. V. Sushko, Y. Shao, J. Liu, C. M. Wang and N. D. Browning, *Nano Lett.*, 2015, **15**, 1177–1182.
- 22 R. Yaokawa, T. Ohsuna, T. Morishita, Y. Hayasaka, M. J. S. Spencer and H. Nakano, *Nat. Commun.*, 2016, **7**, 6–11.
- 23 P. Vogt, P. Capiod, M. Berthe, A. Resta, P. De Padova, T. Bruhn, G. Le Lay and B. Grandidier, *Appl. Phys. Lett.*, 2014, **104**, 4–9.
- 24 C. L. Lin, R. Arafune, K. Kawahara, N. Tsukahara, E. Minamitani, Y. Kim, N. Takagi and M. Kawai, *Appl. Phys. Express*, 2012, **5**, 5–8.
- 25 M. De Crescenzi, I. Berbezier, M. Scarselli, P. Castrucci, M. Abbarchi, A. Ronda, F. Jardali, J. Park and H. Vach, *ACS Nano*, 2016, **10**, 11163–11171.
- 26 R. E. Roman and S. W. Cranford, *Comput. Mater. Sci.*, 2014, **82**, 50–55.
- 27 C. Grazianetti, D. Chiappe, E. Cinquanta, G. Tallarida, M. Fanciulli and A. Molle, *Appl. Surf. Sci.*, 2014, **291**, 109–112.
- 28 Z. Ni, Q. Liu, K. Tang, J. Zheng, J. Zhou, R. Qin, Z. Gao, D. Yu and J. Lu, *Nano Lett.*, 2012, **12**, 113–118.
- 29 G. Le Lay, *Nat. Nanotechnol.*, 2015, **10**, 202–203.
- 30 S. Cahangirov, M. Audiffred, P. Tang, A. Iacomino, W. Duan, G. Merino and A. Rubio, *Phys. Rev. B: Condens. Matter Mater. Phys.*, 2013, **88**, 035432.
- 31 Y. Yao, A. Liu, J. Bai, X. Zhang and R. Wang, *Nanoscale Res. Lett.*, 2016, **11**, 371.
- 32 T. N. Do, G. Gumbus, P. H. Shih, D. Huang, C. W. Chiu, C. Y. Chen and M. F. Lin, *Sci. Rep.*, 2019, **9**, 1–15.
- 33 A. E. Galashev, Y. P. Zaikov and R. G. Vladkyin, *Russ. J. Electrochem.*, 2016, **52**, 966–974.
- 34 A. Y. Galashev and Y. P. Zaikov, *J. Appl. Electrochem.*, 2019, **49**, 1027–1034.
- 35 A. Y. Galashev and K. A. Ivanichkina, *ChemElectroChem*, 2019, **6**, 1525–1535.
- 36 V. Ponce, D. E. Galvez-Aranda and J. M. Seminario, *Phys. Chem. Chem. Phys.*, 2021, **23**, 597–606.
- 37 A. E. Galashev and Y. P. Zaikov, *Russ. J. Phys. Chem. A*, 2015, **89**, 2243–2247.



38 A. E. Galashev, O. R. Rakhmanova and K. A. Ivanichkina, *J. Struct. Chem.*, 2018, **59**, 877–883.

39 W. Rui, W. Shaofeng and W. Xiaozhi, *J. Appl. Phys.*, 2014, **116**, 024303.

40 A. Bourke, R. P. Lynch and D. N. Buckley, *ECS Trans.*, 2013, **53**, 59.

41 H. X. Zhong, R. G. Quhe, Y. Y. Wang, J. J. Shi and J. Lü, *Chin. Phys. B*, 2015, **24**, 087308.

42 Y. Yamada-Takamura and R. Friedlein, *Sci. Technol. Adv. Mater.*, 2014, **15**, 64404.

43 A. Y. Galashev and A. S. Vorob'ev, *J. Solid State Electrochem.*, 2018, **22**, 3383–3391.

44 A. Y. Galashev and K. A. Ivanichkina, *Phys. Lett. A*, 2017, **381**, 3079–3083.

45 A. Curcella, R. Bernard, Y. Borensztein, A. Resta, M. Lazzeri and G. Prévot, *Phys. Rev. B*, 2016, **94**, 1–6.

46 J. F. Justo, M. Z. Bazant and E. Kaxiras, *Phys. Rev. B: Condens. Matter Mater. Phys.*, 1998, **58**, 2539–2550.

47 Y. Jing, Y. Sun, H. Niu and J. Shen, *Phys. Status Solidi B*, 2013, **250**, 1505–1509.

48 X. Yuan, G. Lin and Y. Wang, *Mol. Simul.*, 2016, **42**, 1157–1164.

49 M. Hu, X. Zhang and D. Poulikakos, *Phys. Rev. B: Condens. Matter Mater. Phys.*, 2013, **87**, 1–11.

50 R. Yu, P. Zhai, G. Li and L. Liu, *J. Electron. Mater.*, 2012, **41**, 1465–1469.

51 D. J. Evans and B. L. Holian, *J. Chem. Phys.*, 1985, **83**, 4069–4074.

52 L. A. Selis and J. M. Seminario, *RSC Adv.*, 2019, **9**, 27835–27848.

53 N. Kumar and J. M. Seminario, *J. Phys. Chem. C*, 2016, **120**, 16322–16332.

54 D. E. Galvez-Aranda, V. Ponce and J. M. Seminario, *J. Mol. Model.*, 2017, **23**, 120.

55 R. Clark, M. Von Domaros, A. J. S. McIntosh, A. Luzar, B. Kirchner and T. Welton, *J. Chem. Phys.*, 2019, **151**, 164503.

56 V. Ponce, D. E. Galvez-Aranda and J. M. Seminario, *J. Phys. Chem. C*, 2017, **121**, 12959–12971.

57 J. Petracic and J. Delhomelle, *J. Chem. Phys.*, 2003, **118**, 7477–7485.

58 G. Bussi, D. Donadio and M. Parrinello, *J. Chem. Phys.*, 2007, **126**, 014101, DOI: [10.1063/1.2408420](https://doi.org/10.1063/1.2408420).

59 E. Braun, S. M. Moosavi and B. Smit, *J. Chem. Theory Comput.*, 2018, **14**, 5262–5272.

60 S. Plimpton, *J. Comput. Phys.*, 1995, **117**, 1–19.

61 S. Zhao, Y. Xiong, S. Ma, J. Zhang, B. Xu and J.-J. Kai, *Acta Mater.*, 2021, **219**, 117233.

62 M. M. Ghosh, *J. Nanosci. Nanotechnol.*, 2013, **13**, 2961–2966.

63 O. Folorunso, Y. Hamam, R. Sadiku, S. S. Ray and G. J. Adekoya, *Eng. Solid Mech.*, 2021, **9**, 311–322.

64 K. Sau and T. Ikeshoji, *J. Phys. Chem. C*, 2020, **124**, 20671–20681.

65 Z. Zhuo, X. Wu and J. Yang, *Nanoscale*, 2018, **10**, 1265–1271.

66 G. Kresse and J. Hafner, *Phys. Rev. B: Condens. Matter Mater. Phys.*, 1993, **47**, 558–561.

67 G. Kresse and J. Furthmüller, *Phys. Rev. B: Condens. Matter Mater. Phys.*, 1996, **54**, 11169–11186.

68 J. P. Perdew, K. Burke and M. Ernzerhof, *Phys. Rev. Lett.*, 1996, **77**, 3865–3868.

69 S. Grimme, J. Antony, S. Ehrlich and H. Krieg, *J. Chem. Phys.*, 2010, **132**, 154104.

70 P. E. Blöchl, J. Kästner and C. J. Först, in *Handbook of Materials Modeling*, Springer Netherlands, Dordrecht, 2005, pp. 93–119.

71 S. Fischer and M. Karplus, *Chem. Phys. Lett.*, 1992, **194**, 252–261.

72 G. P. P. Pun and Y. Mishin, *Phys. Rev. B*, 2017, **95**, 224103.

73 R. Vissers, M. A. van Huis, J. Jansen, H. W. Zandbergen, C. D. Marioara and S. J. Andersen, *Acta Mater.*, 2007, **55**, 3815–3823.

74 A. G. Frøseth, R. Høier, P. M. Derlet, S. J. Andersen and C. D. Marioara, *Phys. Rev. B: Condens. Matter Mater. Phys.*, 2003, **67**, 1–11.

